

First Principles Study of Structural, Electronic and Magnetic Interplay in Ferroelectromagnetic Yttrium Manganite

Alessio Filippetti and Nicola A. Hill

Materials Department, University of California

Santa Barbara, CA 93106-5050

Tel. (805) 893-7920

Fax: (805) 893-7221

e-mail: nahill@mrl.ucsb.edu

(February 1, 2008)

We present results of local spin density approximation (LSDA) pseudopotential calculations for the ferroelectromagnet, yttrium manganite (YMnO_3). The origin of the differences between ferroelectric and non-ferroelectric perovskite manganites is determined by comparing the calculated properties of yttrium manganite in its ferroelectric hexagonal and non-ferroelectric orthorhombic phases. In addition, orthorhombic YMnO_3 is compared with the prototypical non-ferroelectric manganite, lanthanum manganite. We show that, while the octahedral crystal field splitting of the cubic perovskite structure causes a centro-symmetric Jahn-Teller distortion around the Mn^{3+} ion, the markedly different splitting in hexagonal perovskites creates an electronic configuration consistent with ferroelectric distortion. We explain the nature of the distortion, and show that a local magnetic moment on the Mn^{3+} ion is a requirement for it to occur.

pacs numbers 75.50.Dd, 71.20.-b, 77.84.-s, 71.15.Mb

Keywords: multiferroic, manganite, crystal field, uniaxial anisotropy, ferroelectricity

I. INTRODUCTION

The observation of colossal magnetoresistance (CMR) in $(\text{La,Ca})\text{MnO}_3$ [1] has prompted a flurry of recent research on this material and related perovskite structure manganites [2]. The majority of the recent research has focused on manganites in which the large (A-site) cation is a rare earth from the left hand side of the lanthanide series. The manganites of these large rare earth ions (lanthanum manganite through dysprosium manganite) all crystallize in the cubic perovskite structure (Figure 1), with the same low temperature orthorhombic distortion and A-type antiferromagnetic ordering of the Mn^{3+} ions.

During the recent studies, many rare earth manganites have been found to show strong coupling between their magnetic and structural, or magnetic and electric order parameters. For example, a magnetically induced structural phase transition has been observed in $\text{La}_{0.83}\text{Sr}_{0.17}\text{MnO}_3$ [3] indicating strong coupling between the local magnetic spin moments and the lattice structure. In $\text{Nd}_{0.5}\text{Sr}_{0.5}\text{MnO}_3$, strong coupling between the magnetic spin moments

and the electronic charge carriers was demonstrated when an electronic metal-insulator transition was induced by an external magnetic field [4]. Indeed the large change in conductivity with applied magnetic field, which causes colossal magnetoresistance is believed to originate from a similar type of phase transition [5].

The strong coupling between magnetic and electric order parameters is of particular interest in the manganites of yttrium and the smaller (holmium through lutetium) rare earths at the right hand side of the lanthanide series. In these materials, the hexagonal perovskite structure (Figure 2) is the lowest energy structure. However the metastable orthorhombic cubic perovskite phase can be regained by annealing at high pressure [6], or by appropriate choice of synthetic method. The phase transition between the stable hexagonal phase and the metastable orthorhombic phase is reconstructive and first order.

In the hexagonal manganites, as in the cubic manganites, superexchange between adjacent Mn^{3+} ions causes anti-ferromagnetic ordering. However in addition to the magnetic ordering, the hexagonal manganites also undergo a phase transition to a non-centrosymmetric low temperature state which has *ferroelectric* ordering. Therefore the hexagonal yttrium and rare-earth manganites belong to the rather small group of materials known as ferroelectromagnets, in which magnetic and ferroelectric ordering occurs simultaneously. Although there are thirteen point groups which permit the occurrence of spontaneous magnetization and spontaneous polarization in the same phase [7], remarkably few ferroelectric materials show any kind (ferro- ferri- antiferro-, etc.) of magnetic ordering. Understanding the fundamental physics that tends to discourage simultaneous ferroelectricity and magnetic ordering is an area of current research activity [8]. And the fact that the ferroelectric hexagonal manganites can be readily transformed to their non-ferroelectric cubic form makes them ideal prototypes for studying this phenomenon.

The goal of the study described in this paper is to explore theoretically the similarities and differences between non-ferroelectric cubic manganites and their ferroelectric hexagonal counterparts. To achieve this goal we evaluate the electronic and magnetic properties of some representative perovskite manganites using a plane wave pseudopotential (PWPP) implementation of density functional theory (DFT) within the local spin density approximation (LSDA). Our choice of theoretical approach is influenced by successful first-principles studies of *non-magnetic* perovskite ferroelectrics [9,10], and by earlier work which elucidated the origins of the differences between related cubic perovskite manganites [11,12]. We calculate the differences between the electronic properties of cubic and hexagonal YMnO_3 to determine the reasons for the lack of ferroelectricity in cubic manganites, and its presence in hexagonal manganites. We also compare our calculated results for cubic YMnO_3 with those for the prototypical cubic perovskite manganite, LaMnO_3 , to establish whether the metastability of the *cubic* phase of YMnO_3 is merely the result of the small size of the yttrium ion, or if electronic factors also play a role.

The remainder of this paper is organized as follows: In Section II we summarize the experimental results for YMnO_3 from the literature. In Section III we briefly describe our plane wave pseudopotential implementation of density functional theory and outline the technical details of the calculations used in this work. In Section IV our results for cubic and hexagonal YMnO_3 are presented, followed by a comparison of the properties of cubic YMnO_3 with those of LaMnO_3 . Our results are summarized in Section V.

II. SUMMARY OF EXPERIMENTAL RESULTS

The literature on the hexagonal manganites is much more limited than that on the cubic perovskite manganites, and modern work focuses largely on yttrium manganite, YMnO_3 . Although yttrium is not a rare earth, it forms a stable trivalent cation with a similar ionic radius to those of the smaller rare earth ions. It is favored over the smaller rare earth ions in research studies for two reasons. First, study of magnetic ordering on the Mn^{3+} ions is more straightforward in YMnO_3 than in the rare earth manganites since there is no perturbation from the rare earth f -electron magnetic moment. In addition, YMnO_3 forms both the hexagonal and orthorhombic phases on solution synthesis at ambient pressure [13] making it particularly appealing for use in a comparative study.

Early (1960s) work on YMnO_3 [13] established the hexagonal phase to be ferroelectric, with the hexagonal perovskite structure and the $P6_3cm$ space group. The hexagonal perovskite structure consists of $ABCACB\dots$ stacking of close packed O layers, with the Mn ions occupying 5-fold coordinated sites, and the rare earth atoms in 7-fold coordinated interstices. The ideal high temperature paraelectric structure consists of two formula units per unit cell and is shown in Figure 2. Since this structure does not occur in the perovskite ferrites it has been suggested that the ability of Mn^{3+} to form 5-fold trigonal bipyramids through dsp^3 hybrid bonding might be a requirement [13]. In addition (not shown in the Figure) at low temperature the MnO_5 bipyramids are slightly rotated around the axis passing through the Mn and parallel to one of the triangular base sides. Early reports of a weak parasitic ferromagnetism [14] were soon shown to be the result of Mn_3O_4 impurity contaminating the powdered phase [15], and weak ferromagnetism was shown to be absent in single crystal samples [15].

Modern studies of hexagonal YMnO_3 have established that the ferroelectricity occurs along the c axis (i.e. $[0001]$) [16,17], with a spontaneous $\mathbf{P} \sim 5.5 \mu\text{C}/\text{cm}^2$. In addition a strong coupling between the ferroelectric and magnetic ordering has been revealed [18]. Although the ferroelectric Curie temperature (914K) is quite different from the Néel temperature (80K), anomalies in the dielectric constant and loss tangent near the Néel temperature are indicative of coupling between the ferroelectric and antiferromagnetic orders. The coupling has been attributed to changes in the phonon spectrum associated with the antiferromagnetic transition [18]. Raman and infra-red spectroscopy of the high temperature paraelectric and low temperature ferroelectric phases show only weak bands in the ferroelectric phase due to the non-centrosymmetry. This indicates that the structural differences between the ferroelectric and paraelectric phases are very small. Non-linear optical spectroscopy [19] shows two types of optical second harmonic spectra of the Mn^{3+} ions in hexagonal YMnO_3 , one from the non-centrosymmetric ferroelectric ordering of charges, and the other caused by the centrosymmetric antiferromagnetic ordering of spins. Partial overlapping between the electronic transitions results in a nonlinear optical polarization which depends on two order parameters. A generalized Ginzburg-Landau formalism has been developed which shows that the second harmonic generation susceptibility is directly proportional to the bilinear combination of both order parameters [20]. Finally, epitaxial thin films of hexagonal YMnO_3 have been grown on (111) MgO and (0001) ZnO:Al/(0001) [16], and explored for use as non-volatile memory devices. YMnO_3 presents some technological advantages over many common ferroelectric perovskites, including lower dielectric constant (~ 20 at room temperature) and non-volatile constituent elements.

In the 1970s, work began on the orthorhombic phase of YMnO_3 . Susceptibility measurements established that orthorhombic YMnO_3 is an antiferromagnet with a Néel temperature of 42K, although significant deviations from Curie-Weiss behavior were seen well above the manganese ordering temperature [6]. A more detailed study [21] concluded that the Mn^{3+} ordering is helical with a propagation wavevector $\mathbf{k} = [0, 0.0786, 0]$ and a helical angle from plane to plane of 14° . Within each plane the ordering is antiferromagnetic.

There has also been some modern work on the orthorhombic phase of YMnO_3 . Attempts have been made to find a synthesis which will produce a larger proportion of the metastable orthorhombic phase [22]. In addition the Raman spectrum of orthorhombic YMnO_3 has been measured and the Raman active phonon modes determined and compared with those of LaMnO_3 [23].

III. COMPUTATIONAL TECHNIQUE

The calculations described in this work were performed using plane wave pseudopotential (PWPP) implementations [24] of density functional theory [25] within the local spin density approximation (LSDA). The accuracy and efficiency of *ab initio* pseudopotential calculations (compared with all-electron calculations) is now well established for spin-polarized magnetic systems, and the PWPP method has been applied to a wide range of magnetic materials [26].

In this work we use both the optimized pseudopotentials developed by Rappe et al. [27] and the Vanderbilt ultra-soft pseudopotentials [28], to reduce the energy cut-off of the plane wave expansion to around 60 and 35 Ry respectively. For La and Y, we constructed scalar-relativistic pseudopotentials, and for Mn and O non-relativistic pseudopotentials were used with the partial non-linear core correction scheme of Louie et al. [29] applied to the Mn ions. The pseudopotentials were tested for transferability by comparing with all-electron calculations for a range of typical atomic and ionic configurations. The pseudo-eigenvalues and total energies were found to be equivalent to the all-electron values to within a few meVs. All pseudopotentials were converted into the usual Kleinman-Bylander form [30], and the absence of ghost states was confirmed using the ghost theorem of Gonze, Käckell and Scheffler [31]. The pseudopotential construction and the total energy calculations used the Perdew-Zunger parameterization [32] of the Ceperley-Alder exchange correlation potential [33] with the von Barth-Hedin interpolation formula [34].

The total energies and band structures were calculated using the CASTEP 2.1 [35,36] and PWSCF ultra-soft pseudopotential programs. For cubic perovskites we used a plane wave cut off of 60 Ry, which corresponds to around 3500 plane waves in a cubic unit cell with lattice constant of around 4 Å. A 6x6x6 Monkhorst-Pack [37] grid was used for all calculations for cubic systems. This led to 10 k-points in the irreducible Brillouin Zone for the high symmetry structures, and a correspondingly higher number for the structures with lower symmetry. In calculations for the hexagonal structure, a 5x5x4 Monkhorst-Pack grid was used, resulting in 18 k-points in the irreducible Brillouin Zone for the high symmetry structures. A variable Gaussian broadening between 1 eV and 0.002 eV was applied to the k-point sampling to speed convergence for metallic systems. For density of states (DOS) calculations we calculated first-principles eigenvalues of a large (≈ 100 in the irreducible Brillouin zone) k-point set, then interpolated using the interpolation scheme of Monkhorst and Pack [37]. We then applied the Gilat-Raubenheimer method [38] to integrate

over this fine mesh. Finally, for the band structure plots, and for use in the tight-binding analysis, symmetry labels along high-symmetry lines were assigned using projection operators for the corresponding irreducible representations.

IV. RESULTS

A. Calculated Electronic Properties of cubic and hexagonal YMnO₃

In this section we compare the electronic properties of YMnO₃ in its metastable cubic perovskite structure with those of the stable hexagonal phase. We begin by calculating the electronic structure for the ideal high symmetry structures, without including magnetic effects, then lower the magnetic symmetry to the hypothetical ferromagnetic and observed antiferromagnetic phases. Finally we introduce structural distortions to simulate the effects of the onset of ferroelectricity. This ability to isolate structural and magnetic distortions is unique to computational studies, and allows identification of the essential microscopic interactions which cause the observed macroscopic behavior.

1. High Symmetry Paramagnetic Structures

First we present the calculated electronic structures for YMnO₃ in the ideal cubic and hexagonal structures, without spin polarization (we call this the paramagnetic (PM) phase).

a. Cubic Figure 3 shows the calculated density of states (DOS) for cubic paramagnetic YMnO₃. We chose a lattice constant of 3.84 Å which corresponds to the average of the lattice constants in the low temperature orthorhombic unit cell. The plotted energy range is from -8 eV to 4 eV, and the lower lying semi-core states have been omitted for clarity. The Fermi level is set to zero. The broad series of bands between approximately -2 and -7 eV arises primarily from the oxygen 2*p* orbitals. Above the oxygen 2*p* bands, and separated from them by an energy gap, are the Mn 3*d* bands. The Mn 3*d* bands are divided into two sub-bands - the lower energy *t*_{2*g*} bands, and the higher energy *e*_{*g*} bands - as a result of the crystal field splitting by the octahedral oxygen anions. The Fermi level lies near the top of the Mn 3*d* *t*_{2*g*} bands and is in a region of high density of states. The large DOS at the Fermi level confirms that the cubic PM structure is unstable, and that a lower energy structure could be achieved by allowing spin-polarization and/or structural distortion.

b. Hexagonal The hexagonal paraelectric structure has three lattice parameters; the usual *a* and *c* parameters plus an internal *u* that gives the distance (in units of *c*) between oxygen and yttrium layers, and is not fixed by the symmetry. In *ideal* hexagonal structures (without tilting of the oxygen octahedra) the atomic positions in crystal coordinates are: Y at (0,0,0) and (0,0, $\frac{1}{2}$), Mn at ($\frac{1}{3}, \frac{2}{3}, \frac{1}{4}$) and ($\frac{2}{3}, \frac{1}{3}, \frac{3}{4}$) O at (0,0, $\frac{1}{4}$), (0,0, $\frac{3}{4}$), ($\frac{1}{3}, \frac{2}{3}, u$), ($\frac{2}{3}, \frac{1}{3}, 1-u$), ($\frac{2}{3}, \frac{1}{3}, \frac{1}{2}+u$) and ($\frac{1}{3}, \frac{2}{3}, \frac{1}{2}-u$), with *u* not fixed by the symmetry. By energy minimization we obtain *a*=3.518 Å, *c*=11.29 Å, and *u*=0.084, in very good agreement with the experimental values *a*=3.539 Å, *c*=11.3(4) Å, and *u*=0.084. This suggests that the oxygen tilting which we are neglecting in these calculations indeed has little effect on the structural properties. Note however that in the ideal, non-magnetic, high symmetry structures, we find that the hexagonal phase is not energetically stabilized over the cubic phase. This indicates that the low temperature structural distortions

and magnetic polarizations which we investigate in the next section are responsible for the stability of the hexagonal phase.

In Figure 4 we show the calculated orbital-resolved DOSs for the non-magnetic hexagonal phase at the LSDA minimum energy lattice parameters. For clarity only the DOS on the *transverse* oxygens is shown since these are most strongly involved in chemical bonding with the Mn ion and will be most important in our later analysis of ferroelectricity. As in the cubic case, the non-magnetic hexagonal phase shows a large DOS at E_F , mostly due to the Mn d states located in a narrow region around E_F . In sharp contrast with the cubic phase, however, the hexagonal crystal field splits the d states into three groups. The d_{xy} and $d_{x^2-y^2}$ orbitals lie on the (0001) plane and are nearly degenerate (only one of them is shown in the Figure). These orbitals point towards the nearby in-plane oxygens (O_P), and so are able to participate in covalent bonding, therefore they form a rather broad band. The d_{xz} and d_{yz} orbitals are also almost degenerate. Their DOSs overlap with those of d_{xy} and $d_{x^2-y^2}$, but are localized in a narrower energy region, since they do not point directly towards oxygens and therefore their bands are not broadened by hybridization. Each orbital of the two doublets is roughly half occupied. Finally, d_{z^2} (shaded gray in the Figure for clarity) is the highest in energy and the least occupied. It points towards the transverse oxygens (O_T) which are the closest ligands to the Mn ions and therefore cause the strongest crystal field destabilization. (The distance between the Mn ion and the transverse oxygens along the c axis is 1.875 Å and that between the Mn ion and the in-plane oxygens is 2.03 Å .) However it is important to note that a certain amount of d_{z^2} charge is hybridized with the O_T p_z states located ~ 5 eV below E_F .

In the next section we will show that these important differences in the splitting of the Mn d bands resulting from the different Mn coordination in the two structures, which are apparent already in the high symmetry paramagnetic phases, have a profound effect on their subsequent electronic, structural and magnetic properties in the realistic spin-polarized structures.

2. High symmetry structural phases with magnetic polarization

Next we calculate the properties of both cubic and hexagonal phases, still with the ideal structural high symmetry, but this time in the experimentally observed antiferromagnetic ground state. In both cases, allowing spin polarization lowers the total energy, consistent with the Stoner model, and introduces magnetic moments onto the Mn ions.

a. Cubic In Figure 5 we show the orbital resolved densities of states on single Mn and O ions, in ideal cubic A-type antiferromagnetic YMnO_3 at the same lattice constant used for the paramagnetic calculations. The A-type AFM phase consists of ferromagnetically aligned (100) planes of Mn ions coupled antiferromagnetically to each other. Due to the exact AFM symmetry, each atom has a corresponding atom in the cell with anti-aligned spin, so the up and down components of DOS are exchanged. The upper plot shows the up-spin and down-spin Mn $3d$ densities of states above and below the x-axis respectively, and the lower plot shows the up-spin oxygen density of states. The down-spin oxygen density of states is not shown since it is very similar to the up-spin. The oxygen density of states in this region derives almost entirely from the oxygen $2p$ orbitals; there is negligible contribution from the O $2s$ orbitals in

the region shown. The densities of states of the d_{xy} , d_{xz} and d_{yz} (not shown) orbitals are very similar. In the absence of the antiferromagnetic ordering these would be identical by symmetry and would form the t_{2g} manifold. Similarly the d_{z^2} and $d_{x^2-y^2}$ bands, from the e_g manifold, are alike. The t_{2g} band is rather narrow for both spin directions, and clearly shows an exchange splitting of around 2 eV. This splitting causes the majority t_{2g} band to be fully occupied while the minority t_{2g} band contains only a small amount of electron density. The e_g band is much broader since the d_{z^2} and $d_{x^2-y^2}$ orbitals are more able to hybridize with their oxygen neighbors. It is roughly half-occupied in the majority case, but completely unoccupied in the minority case. The calculated Mn magnetic moment of around 3 μ_B , significantly reduced from the Hund's rule value of 4 μ_B expected for a d^4 ion, reflects the fact that the exchange splitting is not large enough to produce full spin polarization. It is interesting to note that the region of overlapping energy between the Mn 3d and oxygen 2p states is in fact rather small, with only a small amount of Mn density occurring in the oxygen rich region between around -3 and -9 eV, and vice versa. The similarity between the up- and down- spin oxygen densities of states is a consequence of the small Mn 3d - O 2p overlap.

For comparison, the orbital resolved densities of states in ideal cubic *ferromagnetic* YMnO₃ are shown in Figure 6. The upper plot shows the up-spin and down-spin Mn 3d densities of states above and below the x-axis respectively, and the lower plot shows the up- and down-spin oxygen densities of states. In this case we have plotted only one of the t_{2g} and one of the e_g bands for clarity. The only point that we want to make here is that the densities of states are very similar to those of the antiferromagnetic structure. Therefore as long as spin polarization is allowed, the electronic structure is not very sensitive to the *relative* polarization of neighboring Mn ions.

b. Hexagonal The paraelectric hexagonal structure contains two Mn ions per unit cell, allowing studies of FM and AFM spin orientations without employing supercells. We find that the AFM phase is slightly lower in energy than the FM phase, as is the case in experiment. We focus on the AFM phase in what follows although, as we saw already in the cubic case, the spin ordering is not essential for our arguments. The properties that we consider here are determined by the local (i.e. internal to the oxygen cage) spin polarization rather than by long-range magnetic ordering.

In contrast to the non-spin-polarized phase, in which the d_{xz} , d_{yz} and d_{xy} , $d_{x^2-y^2}$ doublets were roughly half occupied, here the Stoner exchange produces a ~ 2.5 eV energy splitting that causes these four orbitals to become almost completely spin polarized (Figure 7). Their total up and down charges are indeed 3.93 and 0.47 electrons, respectively, while the occupation numbers of $d_{z^2}^\uparrow$ and $d_{z^2}^\downarrow$ orbitals are 0.53 and 0.30 electrons. The resulting magnetic moment on Mn (3.7 μ_B) is less than the 4 μ_B Hund's rule value because of the hybridization of $d_{z^2}^\uparrow$ with O_T p_z states, and of d_{xy} and $d_{x^2-y^2}$ with O_P p_x and p_y states. However it is larger than the value calculated for the cubic case because of the larger exchange splitting occurring here. A non-negligible magnetic moment, $M=0.15 \mu_B$, is also present on O_P , driven by exchange with the d_{xy} and $d_{x^2-y^2}$ orbitals, whereas the magnetization of O_T is almost vanishing, due to the AFM symmetry (for $u=0$ it would be exactly zero).

The large spin splitting does not manage to open a gap. Indeed there is a tiny DOS at E_F , to which d_{xy} and $d_{x^2-y^2}$ orbitals from Mn, and p_x and p_y orbitals from O_P contribute. This means that the bands crossing E_F come completely from orbitals oriented in the $x - y$ plane (the tilting of the oxygen cages in the ferroelectric structure is

probably sufficient to open an energy gap). The mainly planar distribution of the charge density is also evident from the band energies shown in Figure 8, calculated within the $k_z=0$ plane of the Brillouin zone (left panel), and along [0001] (right panel). Only one band crosses E_F at $k_z=0$, and its orbital character is a mix of d_{xy}^\dagger and $d_{x^2-y^2}^\dagger$ states from Mn, and p_x^\dagger and p_y^\dagger states from O_P. The band energies are extremely flat along [0001], as is typical for a strongly layered compound. The system can be described as a poor metal in the $x-y$ plane, and as an insulator perpendicular to it. If we discard the first unoccupied bands coming from in-plane orbitals, we obtain a one-dimensional ‘pseudogap’ of ~ 2 eV between occupied O_T p and empty Mn d_{z^2} states, similar to the energy gap present between occupied oxygen states and empty transition metal d states in classic ferroelectric perovskite oxides such as BaTiO₃.

3. Effects of ferroelectric distortion on the electronic properties of cubic and hexagonal structures

Finally we investigate the sensitivity of the charge distribution to atomic displacements by moving the Mn and in-plane oxygen atoms in opposite directions along the c and z axes in hexagonal and cubic phases respectively.

The results for the hexagonal structure are shown in Figure 9. Note that since the electric polarization occurs along the c axis, and the bipyramidal tilting does not alter significantly the features of this compound, the paraelectric structure without the addition tilting is a sufficient starting point for the purpose of studying the nature of the ferroelectric displacement. For clarity, only the Mn orbitals most involved in the change of hybridization (i.e. d_{xz} and d_{z^2}) are shown. The change of DOS upon distortion is very evident. The Mn d DOS is shifted down by ~ 2 eV and is strongly hybridized with the O_T p states that are localized in a ~ 1 eV wide energy region. The atomic displacements increase the overlap of d_{z^2} and O_T p_z orbitals, inducing a pd_σ hybridization, and the overlap of d_{xz} and d_{yz} with O_T p_x and p_y orbitals, increasing the pd_π hybridization. Note that very similar changes in hybridization with ferroelectric displacement are seen in the prototypical ferroelectric BaTiO₃ [39]. However in BaTiO₃ all the Ti $3d$ orbitals are formally empty, and so displacement in *any* direction causes an energy lowering rehybridization as the oxygen ions transfer charge into the empty d orbitals. By contrast, the ferroelectricity in YMnO₃ is strongly uniaxial because only the d_{z^2} orbital is empty. Since the majority spin d_{xz} and d_{yz} orbitals are almost completely filled, their changes of hybridizations with oxygen on displacement, although significant, do not contribute to a change in electric polarization.

The markedly different results which we obtain for the cubic structure are shown in Figure 10. Again only those orbitals most affected by the distortion (Mn d_{z^2} and d_{xz} and O_T) are shown. The changes in DOS on distortion are much less pronounced and quite different in character from those which we found for the hexagonal phase. The most obvious change is a destabilization of the d_{xz} band which results from the larger crystal field repulsion as the Mn is moved closer to the transverse oxygens along the z axis. Since the d_{xz} orbitals are part of the filled t_{2g} manifold they are unable to lower their energy by rehybridization with the oxygen $2p$ states, therefore the only contribution to their energetics is the unfavorable crystal field repulsion. Note that a typical Jahn-Teller distortion, in which the oxygens along the z axis move *away* from the cation, would have the opposite effect. In addition there is a slight broadening and shift down in energy of the d_{z^2} band, which, since it was originally partly unoccupied, is now better able to accept

charge density from the oxygen ligand that it has moved closer to. There is an almost rigid shift of the oxygen $2p$ bands to lower energy relative to the Fermi energy. This in fact a consequence of the shift of the Fermi level to higher energy due to the destabilization of the Mn $3d$ bands. The fact that the form of the oxygen bands does not change significantly is an indication that rehybridization is minimal.

B. Comparison of the electronic properties of cubic YMnO_3 and LaMnO_3

Finally we briefly compare our calculated band structures of YMnO_3 in its metastable cubic perovskite structure, with those of the prototypical cubic manganite, LaMnO_3 . The purpose of this section is to determine whether there are any important differences between the *electronic* properties of cubic YMnO_3 and LaMnO_3 which might explain why the cubic phase is stable in LaMnO_3 but metastable in YMnO_3 . (Note that the cubic phase does not support ferroelectricity for either compound, therefore since LaMnO_3 does not form in the hexagonal structure it is *never* ferroelectric.) In fact we will find that the band structures of cubic YMnO_3 and LaMnO_3 are very similar, and therefore conclude that LaMnO_3 only forms in the cubic phase, whereas YMnO_3 can be either cubic or hexagonal (and therefore ferroelectric) because the yttrium ion is smaller than the lanthanum ion.

First we report in Table II the relative energies of the paramagnetic (PM), ferromagnetic (FM) and A-type (AFM) phases of cubic YMnO_3 and LaMnO_3 . The relative energies of FM and AFM phases of LaMnO_3 are taken from Ref. [12] and those for YMnO_3 were calculated in this work. The most important feature for our purposes is that the relative orderings of the states is the same in YMnO_3 as in LaMnO_3 . It is also striking that in both cases the ferromagnetically ordered state is the most stable phase. This has been pointed out previously for LaMnO_3 [12], and the relationship between the observed Jahn-Teller distortion and the resulting A-type antiferromagnetic ground state is well understood [41]. Also, in both cases the calculated magnetic moment is about $3.0 \mu_B$ per Mn for the cubic FM and AFM structures, lower than the spin-only value of $4 \mu_B$ for the Mn^{3+} ion as discussed earlier. The similarity in magnetic moment indicates similar amounts of spin-polarization and hybridization in both cases.

Figure 11 shows the band structures of cubic PM YMnO_3 and LaMnO_3 plotted along the high symmetry axes of the simple cubic Brillouin Zone. The Fermi level is set to 0 eV in both cases. The broad O $2p$ bands between around -2 and -7 eV can be seen clearly in both materials, with the Mn $3d$ bands above them, separated by an energy gap. In LaMnO_3 , the Mn $3d$ bands are largely separated in energy at each k -point from the next highest energy bands, which are the La $5d$ bands. The highlighted lines in the LaMnO_3 band structure plots accentuate the upper and lower Mn $3d$ bands, which have a similar form to each other and have been seen in other cubic perovskite manganites (see Refs. [11] and [12].) This indicates a ‘universality’ in the manganite structure throughout the cubic perovskite manganite series, which is independent of the identity of the large cation. The same structure for the upper and lower Mn $3d$ bands can also be identified in the YMnO_3 band structure, however the Mn $3d$ bands are slightly broader than those in LaMnO_3 because the smaller lattice constant results in greater Mn $3d$ - O $2p$ overlap. The smaller lattice constant, and correspondingly larger crystal field repulsion, is also responsible for the larger $t_{2g} - e_g$ splitting which can be clearly seen at the Γ point. In addition the Y $4d$ bands are lower in energy than the La $5d$ bands. These factors result

in the lower part of the Y $4d$ bands intersecting the upper part of the Mn $3d$ bands in some regions of the Brillouin zone, making the universal structure less well-defined.

To quantify any differences between cubic PM YMnO₃ and LaMnO₃, we performed tight-binding analyses of the Γ to X regions of the respective band structures. Tight-binding parameters were obtained by non-linear-least-squares fitting [40] to the calculated *ab initio* energies at the high symmetry Γ and X points, and at 19 points along the Δ axis. The tight-binding parameters thus obtained are given in Table I. In both cases a good (root mean square (RMS) deviation from the *ab initio* energies of 0.20) fit was obtained by including only oxygen $2s$ and $2p$ and Mn $3d$ orbitals in the basis set, since we find no significant covalent bonding between the A cation and either the oxygen $2p$ or the Mn $3d$ orbitals. This is consistent with an early proposal by Goodenough [41] that the magnetic properties of the rare earth manganites are determined by the Mn $3d$ - O $2p$ hybridization only. The parameters for YMnO₃ are similar to those for LaMnO₃, except for an increase of around 10 % in the Mn $3d$ - O nearest neighbor overlaps. This is a consequence of the smaller lattice constant in YMnO₃, and results in the slightly broader Mn $3d$ bands noted above.

To test the effect of size on the electronic properties, we also calculated the properties of cubic paramagnetic YMnO₃ at the experimental LaMnO₃ lattice constant of 3.95 Å. The resulting band structure of this hypothetical structure (not shown) is qualitatively similar to that of YMnO₃ at the true experimental lattice constant, except for a slight narrowing of the bandwidths as a result of the reduced overlap between the atomic wavefunctions, and a reduced t_{2g} - e_g splitting as a result of the lower crystal field repulsion.

We find that introduction of spin polarization causes the same kinds of changes in both compounds, therefore the conclusions drawn from analysis of the paramagnetic band structures continue to be valid. Figure 12 shows the up and down-spin band structures for YMnO₃ and LaMnO₃ along the high symmetry axes of the simple cubic Brillouin Zone. (We chose the ferromagnetic (FM) phases for simplicity in interpreting the band structures; as discussed above, we are interested in the effects of spin polarization rather than the nature of the ordering between magnetic moments.)

First we examine the up- and down-spin LaMnO₃ band structures, and compare with the PM LaMnO₃ band structures to determine the changes which spin polarization causes in a ‘conventional’ manganite. The states which correspond to non-magnetic atoms are unchanged from the paramagnetic state, and are identical for up- and down-spin electrons. For example, the dispersion of the lowest O $2p$ band is very similar for up- and down-spin, and for the PM phase. Also the La $5d$ bands, which were above the Mn $3d$ bands in the PM state are unchanged in form and energy. The characteristic perovskite manganite Mn $3d$ pattern which we remarked on earlier persists in the FM phase, appearing around 2 eV higher for the down-spin electrons than for the up-spin because of the exchange splitting. The up-spin Mn $3d$ and O $2p$ bands are strongly hybridized and there is no gap between them. However, the down-spin Mn $3d$ are split off from the O $2p$ bands by a larger gap than in the PM case. As a result, the Mn $3d$ bands occupy the same energy region as the unoccupied La $5d$ bands. The Fermi level cuts through the very bottom of the down-spin Mn $3d$ bands, and the conduction band is occupied almost entirely by up-spin electrons, indicating half-metallic behavior.

Finally we compare the up- and down-spin YMnO₃ band structures. The first notable feature is that the non-magnetic Y $4d$ bands and O $2p$ bands are very similar for *both* up- and down- spin. This is because the exchange

interaction in this hypothetical ferromagnetic YMnO₃ structure does not remove the gap between the majority Mn d bands and the O $2p$ band. (By contrast, in LaMnO₃ the higher O $2p$ bands overlap with the majority Mn $3d$ bands and therefore show a polarization dependence). This is again the result of the smaller lattice constant in YMnO₃, which destabilizes the unfavorable FM interactions compared with those in LaMnO₃, where the Mn ions are further apart. Both up- and down-spin Mn $3d$ bands show the characteristic perovskite manganite features (most noticeable in this case along the M-R-X directions) which we noted earlier in our discussions of the PM band structures.

The strong similarities between the calculated properties of cubic YMnO₃ and LaMnO₃ that we have presented in this section confirm that the observed differences between the properties of hexagonal and cubic manganites are merely the result of the different sizes of the large cations in the two materials stabilizing different structures, and not due to any additional covalent bonding effects.

V. CONCLUSIONS

In summary, the formal similarity of d^4 Mn³⁺ in hexagonal and cubic YMnO₃ does not prevent the two phases from showing quite different properties. In particular, the difference between hexagonal and cubic field symmetry induces a very different charge distribution. In cubic perovskites, the Mn³⁺ ion has partially occupied e_g states. This creates an instability relieved by Jahn-Teller distortion and the ordering of Mn orbitals on the (001) plane. Both Jahn-Teller and orbital ordering tend to favor structural configurations that keep Mn and O aligned on the same plane, and therefore do not result in ferroelectricity. In the hexagonal perovskites, the crystal field produces an ordering of d states that leaves the d_{z^2} orbital mostly unoccupied, and thus able to hybridize with the p_z orbital of the transverse oxygen. This charge environment favorable to electric polarization along the c axis is only realized in condition of spin-polarization, not for the non-magnetic hexagonal phase. Thus, in hexagonal YMnO₃ the spin-polarization is actually the factor which enables the ferroelectricity. Finally, we emphasize that the transition from the AFM to the paramagnetic phase above $T_N=80$ K (i.e. well below the critical temperature of the ferroelectric phase), does not invalidate our picture, since it is the local spin-polarization of Mn³⁺ that matters, independently of the actual presence (or absence) of spin ordering. Note also that there are no fundamental differences between the electronic structures of metastable cubic YMnO₃ and the prototypical stable cubic manganite, LaMnO₃. Therefore the metastability of the cubic perovskite phase in YMnO₃ is simply the result of the smaller size of the A cation which is unable to stabilize the cubic phase.

VI. ACKNOWLEDGMENTS

The authors acknowledge many useful discussions with Profs. Warren Pickett and Karin Rabe. We thank the authors of CASTEP for providing us with their software package, and Umesh Waghmare for implementing the extension to metallic systems. Funding for this work was provided by the National Science Foundation, grant numbers DMR-9973076 and DMR 9973859. Calculations have been carried out on the IBM SP2 machine of the MHPCC Supercomputing Center in Maui, HI.

-
- [1] S. Jin, T.H. Tiefel, M. McCormack, R.A. Fastnacht, R. Ramesh and L.H. Chen, *Science* **264**, 413 (1994).
- [2] See for example Proceedings of the 41st Annual Conference on Magnetism and Magnetic Materials, Atlanta, GA, 1996 (in *J. Appl. Phys.* vol **81**,8 (1997)), and references therein.
- [3] A. Asamitsu, Y. Moritomo, Y. Tomioka, L. Arima and Y. Tokura, *Nature* **373**, 407 (1995).
- [4] H. Kuwahara, Y. Tomioka, A. Asamitsu, Y. Moritomo and Y. Tokura, *Science* **270**, 961 (1995).
- [5] H. Kuwahara, Y. Tomioka, Y. Moritomo, A. Asamitsu, M. Kasai, R. Kumai and Y. Tokura, *Science* **272**, 80 (1996).
- [6] W.E. Wood, A.E. Austin, E.W. Collins and K.C. Brog, *J. Phys. Chem. Solids* **34**, 859 (1973).
- [7] H. Schmid, *Ferroelectrics* **162**, 317 (1994).
- [8] N.A. Hill, *J. Phys. Chem. B.*, **104**, 6694-6709 (2000).
- [9] U.V. Waghmare and K.M. Rabe, *Phys. Rev. B* **55**, 6161 (1997).
- [10] R.E. Cohen and H. Krakauer, *Ferroelectrics* **136**, 95 (1992).
- [11] N.A. Hill and K.M. Rabe, *Phys. Rev. B.* **59**, 8759 (1999)
- [12] W.E. Pickett and D.J. Singh, *Phys. Rev. B* **53**, 1146 (1996).
- [13] H.L. Yakel, W.C. Koehler, E.F. Bertaut and E.F. Forrat, *Acta. Cryst.* **16** 957 (1963).
- [14] E.F. Bertaut, R. Pauthenet and M. Mercier, *Phys. Lett.* **7**, 110 (1963).
- [15] E.F. Bertaut, R. Pauthenet and M. Mercier, *Phys. Lett.* **18**, 13 (1965).
- [16] N. Fujimura, T. Ishida, T. Yoshimura, and T. Ito, *App. Phys. Lett.* **69**, 1011 (1996).
- [17] S. H. Kim, S. H. Lee, T. H. Kim, T. Zyung, Y. H. Jeong, and M. S. Jang, *Cryst. Res. Technol.* **35**, 19 (2000).
- [18] Z.J. Huang, Y. Cao, Y.Y. Sun, Y.Y. Xue and C.W. Chu, *Phys. Rev. B* **56**, 2623 (1997).
- [19] D. Fröhlich, St. Leute, V.V. Pavlov and R.V. Pisarev, *Phys. Rev. Lett.* **81**, 3239 (1998).
- [20] D. Sa, R. Valentí and C. Gros, cond-mat/9910283, accepted for publication in *European Journal of Physics B*.
- [21] S. Quezel, J. Rossat-Mignod and E.F. Bertaut, *Sol. Stat. Comm.* **14**, 941 (1974).
- [22] H.W. Brinks, H. Fjellvåg and A. Kjekshus, *J. Sol. Stat. Chem.* **129**, 334 (1997).
- [23] M.N. Iliev, M.V. Abrashev, H.-G. Lee, V.N. Popov, Y.Y. Sun, C. Thomsen, R.L. Meng and C.W. Chu, *Phys. Rev. B* **57**, 2872 (1998).

- [24] M.T. Yin and M.L. Cohen, Phys. Rev. B **26**, 5668 (1982).
- [25] P. Hohenberg and W. Kohn, Phys. Rev. **136**, 864 (1964);
W. Kohn and L.J. Sham, Phys. Rev. **140**, 1133 (1965).
- [26] see for example T. Sasaki, A.M. Rappe and S.G. Louie, Phys. Rev. B **52**, 12760 (1995) (ferromagnetic Ni and Fe), S.P. Lewis, P.B. Allen and T. Sasaki, Phys. Rev. B **55**, 10253 (1997) (antiferromagnetic CrO₂) and N.A. Hill and K.M. Rabe, Phys. Rev. B. **59**, 8759 (1999) (perovskite manganites).
- [27] A.M. Rappe, K.M. Rabe, E. Kaxiras and J.D. Joannopoulos, Phys. Rev. B **41**, 1227 (1990).
- [28] D. Vanderbilt, Phys. Rev. B **32**, 8412 (1985).
- [29] S.G. Louie, S. Froyen and M.L. Cohen, Phys. Rev. B **26**, 1738 (1982).
- [30] L. Kleinman and D.M. Bylander, Phys. Rev. Lett. **48**, 1425 (1982).
- [31] X. Gonze, P. Käckell and M. Scheffler, Phys. Rev. B **41**, 12264 (1990).
- [32] J.P. Perdew and A. Zunger, Phys. Rev. B **23**, 5048 (1981).
- [33] D.M. Ceperley and B.J. Alder, Phys. Rev. Lett. **45**, 566 (1980).
- [34] U. von Barth and L. Hedin, J. Phys. C **5**, 1629 (1972).
- [35] M.C. Payne, M.P. Teter, D.C. Allan, T.A. Arias and J.D. Joannopoulos, Rev. Mod. Phys. **64**, 1045 (1992).
- [36] M.C. Payne, X. Weng, B. Hammer, G. Francis, U. Bertram, A. de Vita, J.S. Lin, V. Milman and A. Qteish, unpublished.
- [37] H.J. Monkhorst and J.D. Pack, Phys. Rev. B **13**, 5188 (1976).
- [38] G. Gilat and L.C. Raubenheimer, Phys. Rev. **144**, 390 (1966).
- [39] A. Filippetti and N.A. Hill, submitted to Phys. Rev. B
- [40] L.F. Mattheiss, Phys. Rev. B **6**, 4718 (1972).
- [41] J.B. Goodenough, Phys. Rev. **100**, 564 (1955).

Figure Captions

FIG. 1. The ideal cubic perovskite structure. The small B cation (in black) is at the center of an octahedron of oxygen anions (in gray). The large A cations (white) occupy the unit cell corners.

FIG. 2. The ideal hexagonal perovskite structure. The small B cation (in black) is five-fold coordinated by oxygen anions (in gray). The dashed lines indicate the oxygen pentahedra. The large A cations (white) occupy seven-fold coordinated sites.

FIG. 3. Calculated density of states for cubic paramagnetic YMnO_3 .

FIG. 4. Orbital resolved densities of states for Mn and transverse oxygen in the paraelectric non-magnetic phase of hexagonal YMnO_3 . Only one DOS for each of the nearly degenerate pairs of orbitals ($d_{xy}, d_{x^2-y^2}$) and (d_{xz}, d_{yz}) is shown.

FIG. 5. Orbital resolved densities of states on single Mn and O atoms in cubic antiferromagnetic YMnO_3 .

FIG. 6. Orbital resolved density of states in cubic ferromagnetic YMnO_3 .

FIG. 7. Orbital resolved DOS of a single Mn ion (top panel), in-plane oxygen O_P (middle), and transverse oxygen O_T (bottom) in the paraelectric AFM phase of hexagonal YMnO_3 . p^u and p^d indicate up and down components of O p DOS, respectively.

FIG. 8. Band energies of paraelectric AFM hexagonal YMnO_3 . $Q=\pi/a (0, 2/3^{1/2}, 0)$, $P=\pi/a (1, 1/3^{1/2}, 0)=\Gamma$.

FIG. 9. Orbital-resolved DOS for single Mn and O in hexagonal AFM YMnO_3 . The upper panel is for the paraelectric structure, the lower for the structure with Mn and O displaced along the c axis, in the fashion of a ferroelectric distortion.

FIG. 10. Orbital-resolved DOS for single Mn and O in cubic A-type AFM YMnO_3 . The upper panel is for the paraelectric structure, the lower for the structure with Mn and O displaced along the z axis, in the fashion of a ferroelectric distortion.

FIG. 11. Calculated band structures for cubic paramagnetic LaMnO_3 and YMnO_3 along the high symmetry axes of the Brillouin Zone. The highlighted lines in the band structure plots accentuate the upper and lower Mn $3d$ bands, which have a similar form to each other and to those of other perovskite manganites.

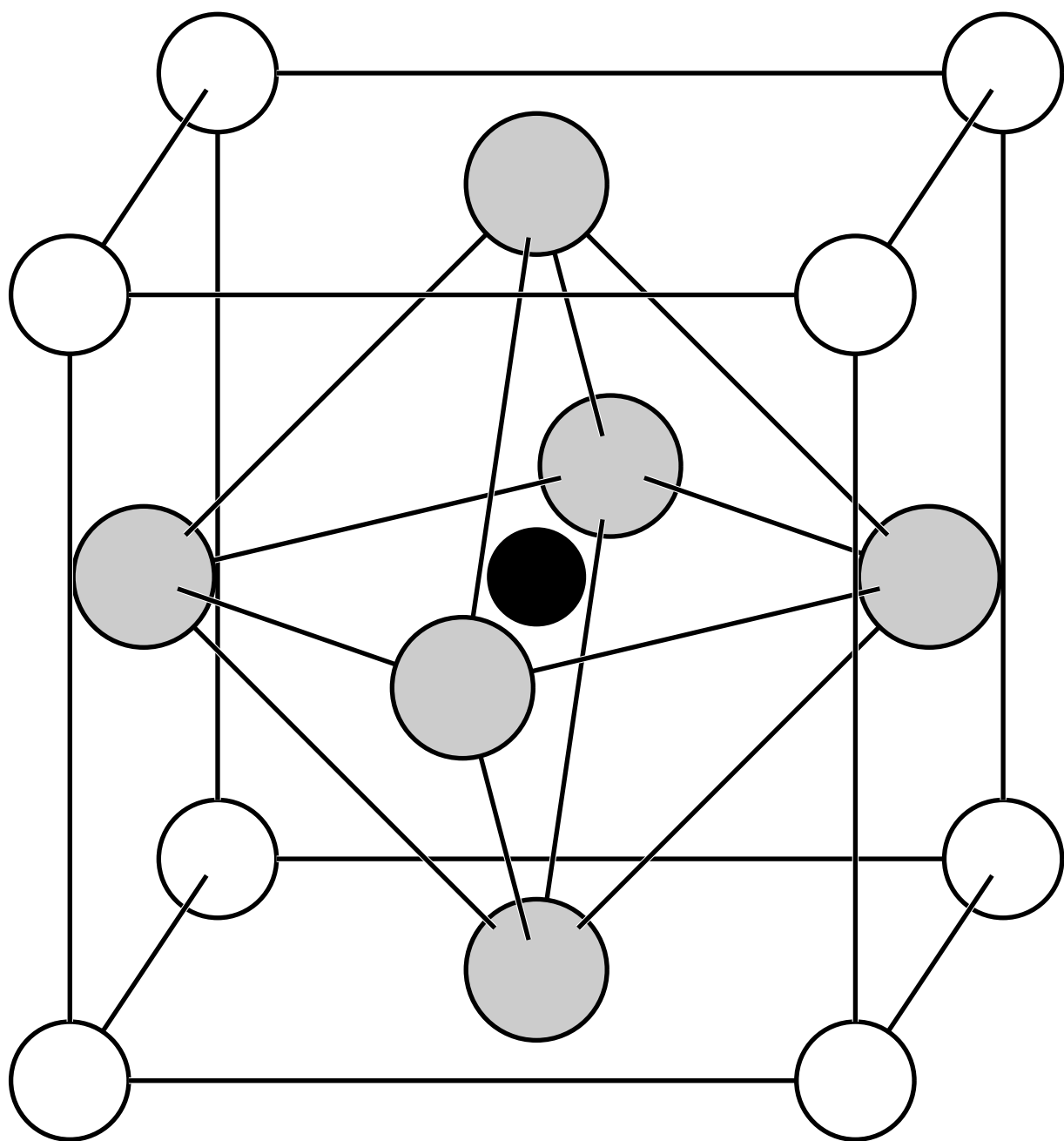
FIG. 12. Up- and down-spin band structures for cubic LaMnO_3 and YMnO_3 along the high symmetry axes of the Brillouin Zone.

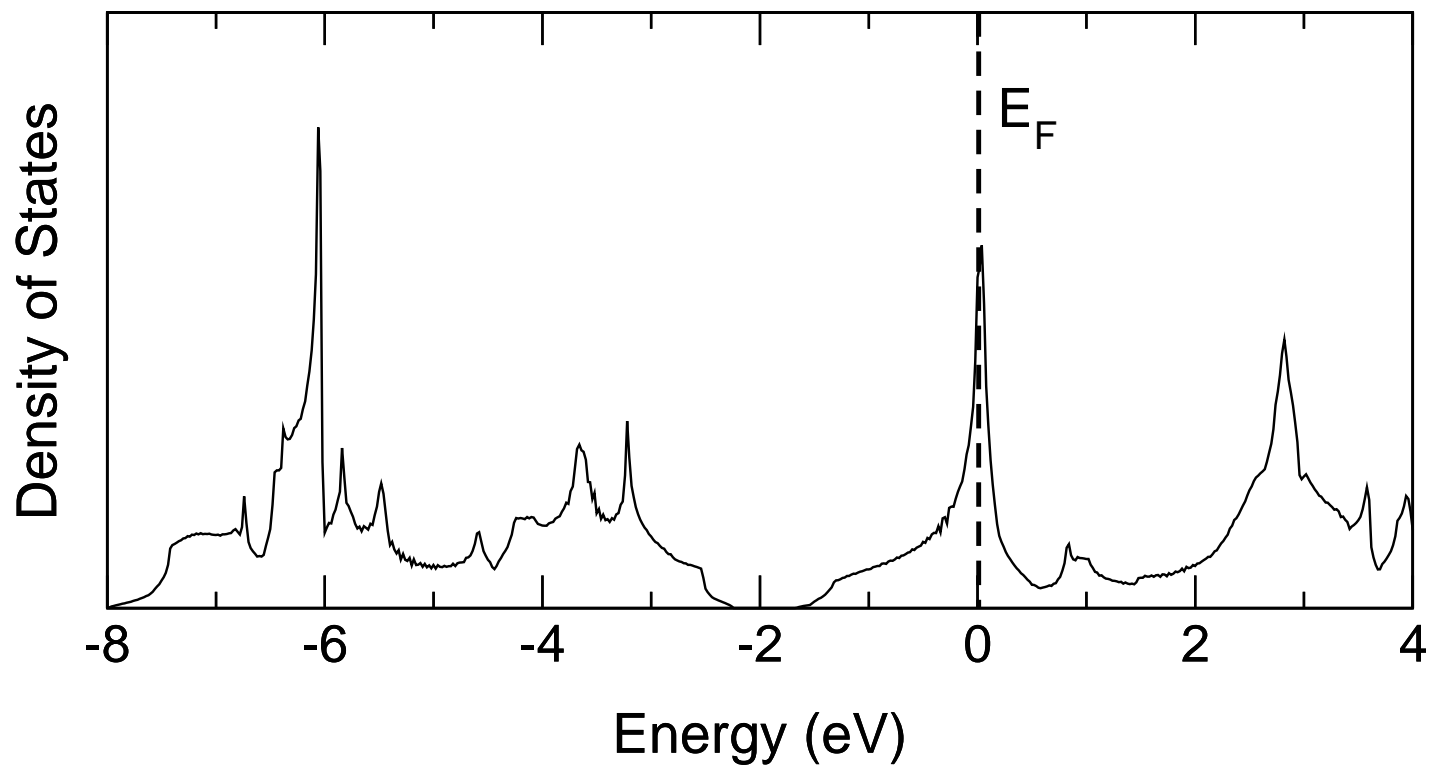
	LaMnO ₃	YMnO ₃
E_{O2s}	-17.836376	-17.9649
E_{O2p}	-4.514022	-4.7382
E_{Mn3d}	-1.191285	-1.4097
$V_{O2s-O2s}$	-0.243683	-0.2461
$V_{(O2p-O2p)\sigma}$	0.620568	-0.7167
$V_{(O2p-O2p)\pi}$	-0.063466	-0.1069
$[V_{(O2p-O2p)\sigma}]_2$	0.182635	0.1688
$[V_{(O2p-O2p)\pi}]_2$	0.082951	0.0620
$V_{O2s-Mn3d}$	-1.735814	-1.9711
$V_{(O2p-Mn3d)\sigma}$	-1.838490	-2.0601
$V_{(O2p-Mn3d)\pi}$	0.878961	1.0837
$V_{(Mn3d-Mn3d)\delta}$	0.066346	0.0488

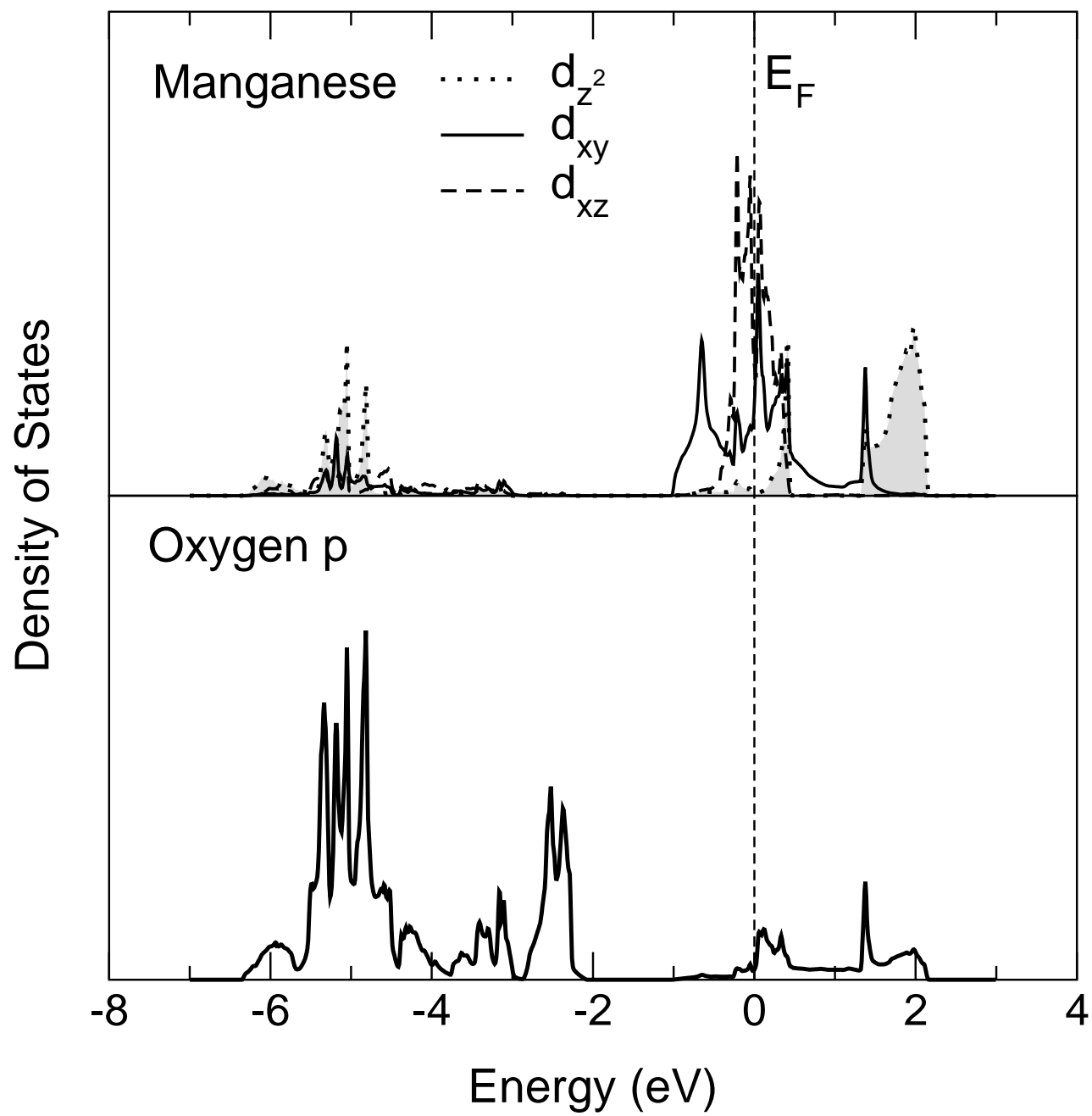
TABLE I. Tight-binding parameters (in eV) for cubic LaMnO₃ and YMnO₃ obtained by non-linear-least-squares fitting to the *ab initio* eigenvalues along Γ to X. E indicates an orbital energy, and V an inter-atomic transfer integral. All transfer integrals are between nearest neighbors, except those with the subscript ‘2’ which are between next nearest neighbors. Only the parameters listed in the table were allowed to be non-zero in the fitting procedure.

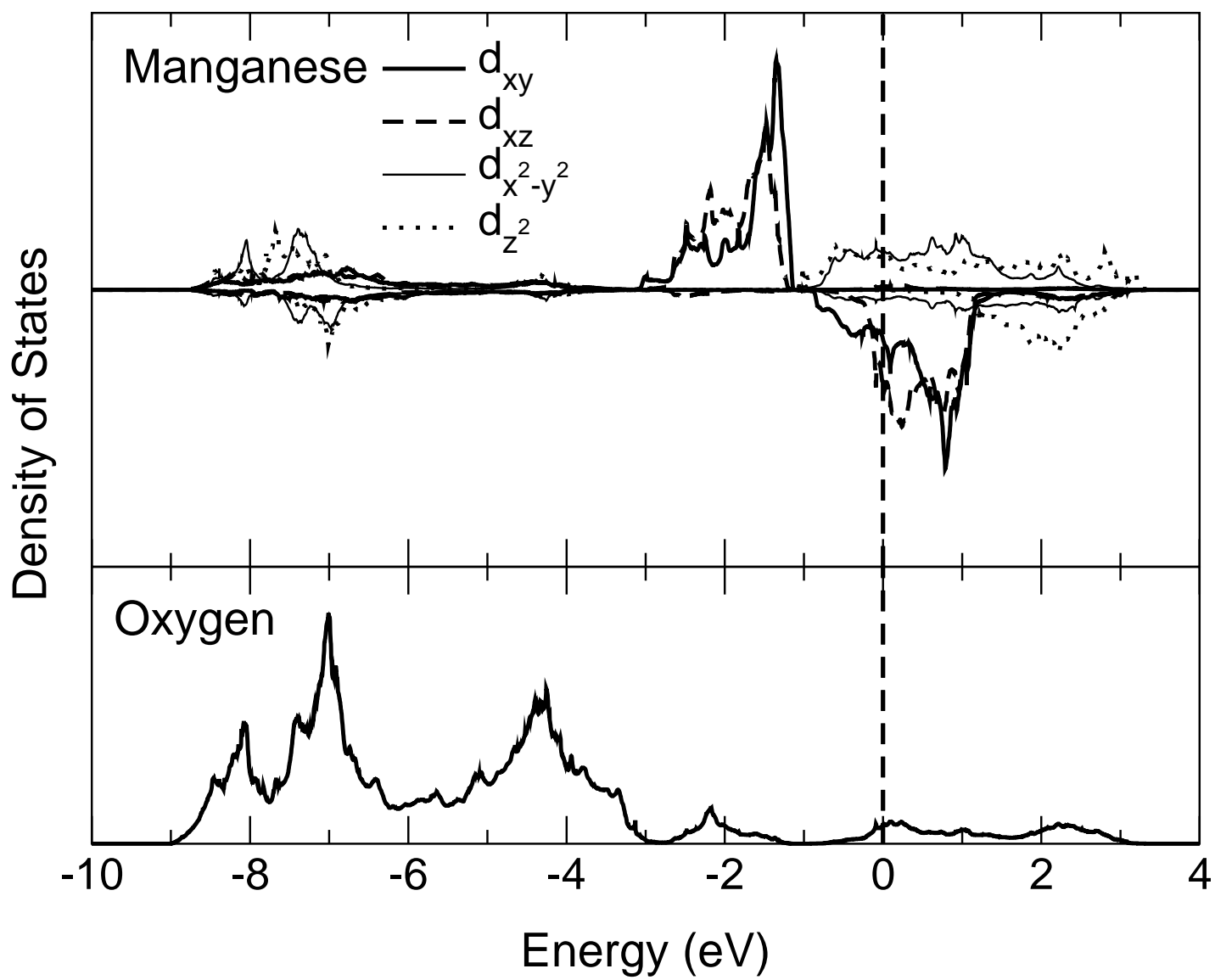
	YMnO ₃	LaMnO ₃
FM	0	0
A-AFM	+140 meV	+110 meV
PM	+0.70 eV	+1.16 eV

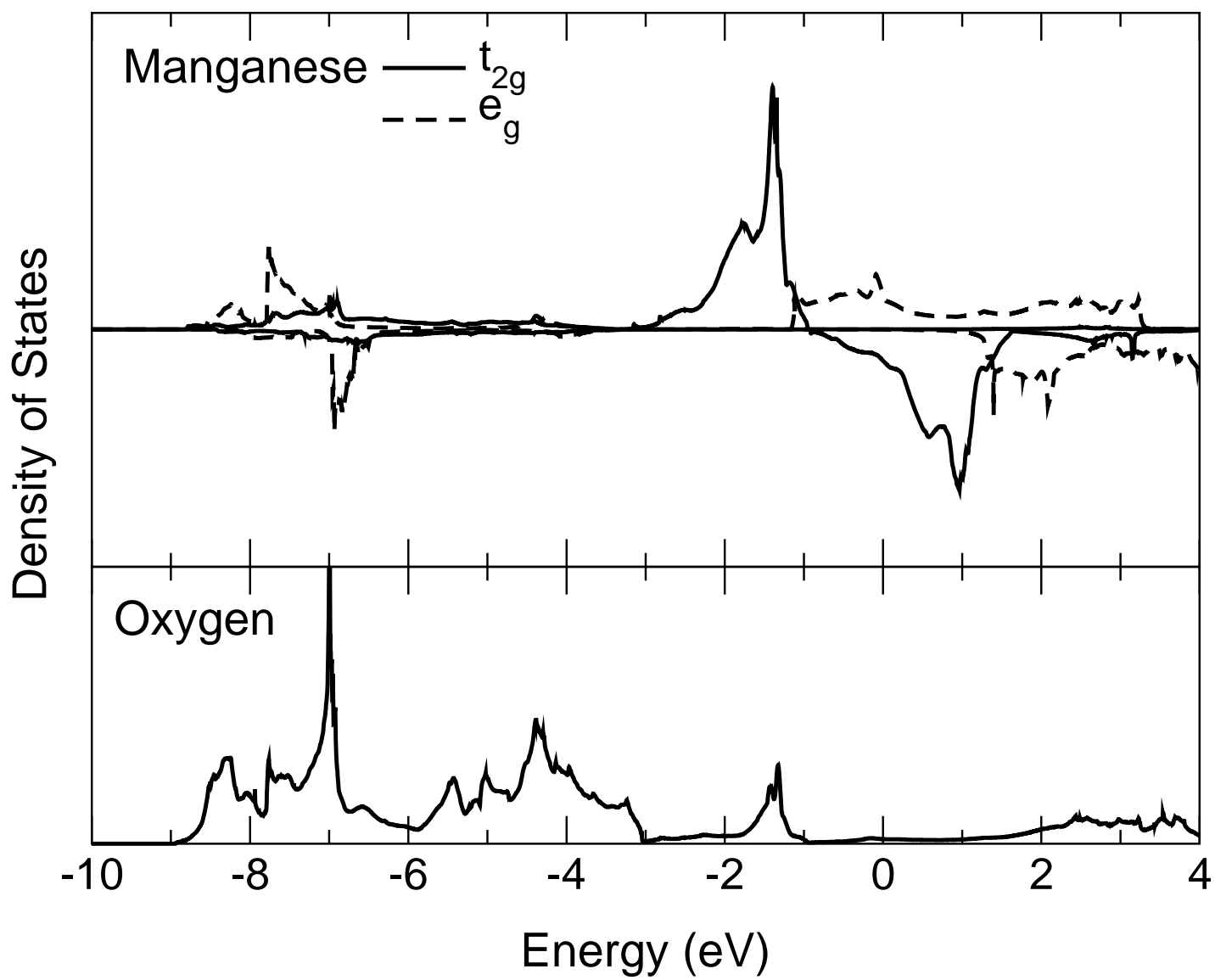
TABLE II. Relative energies of different magnetic phases in cubic paramagnetic YMnO₃ and LaMnO₃.



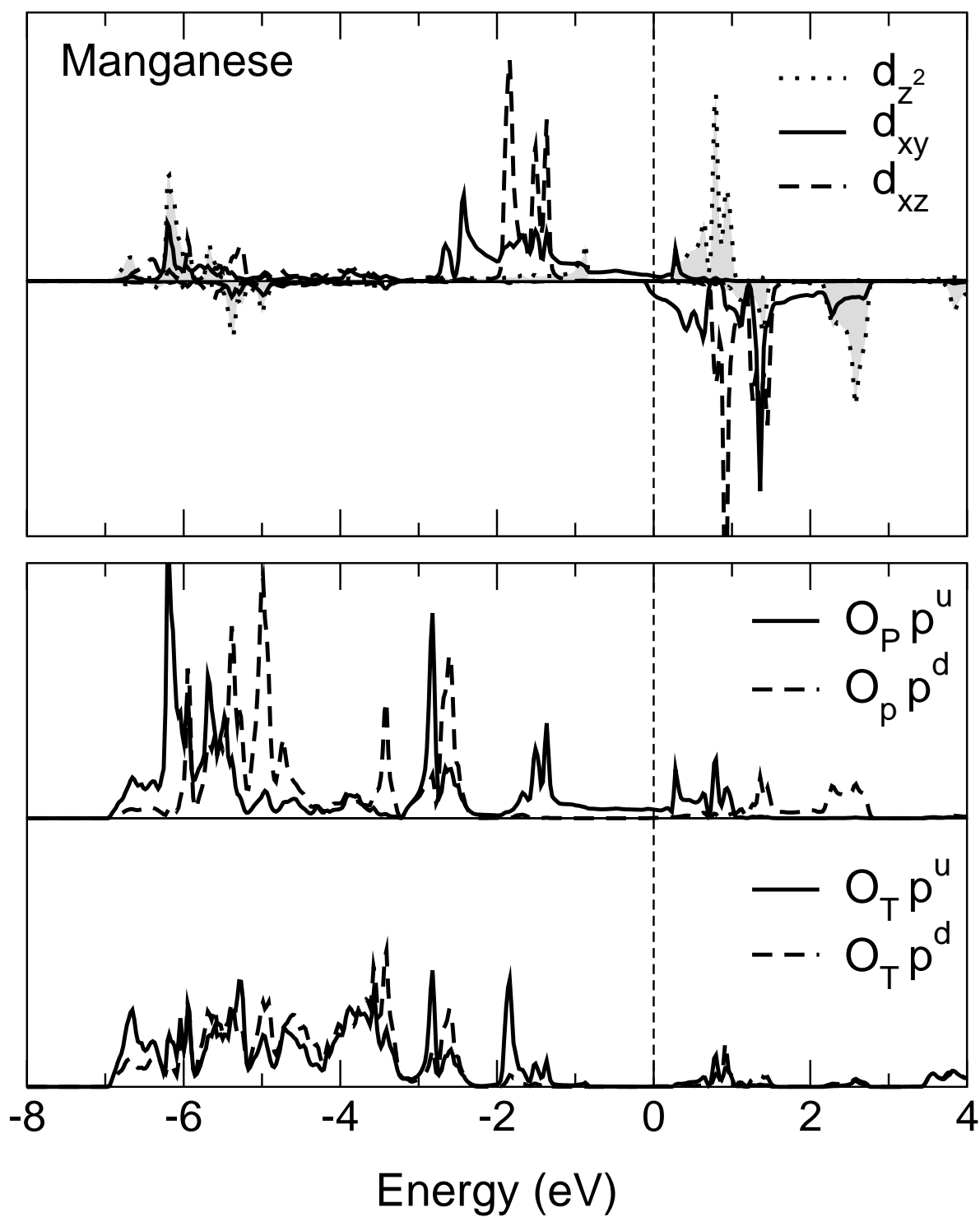


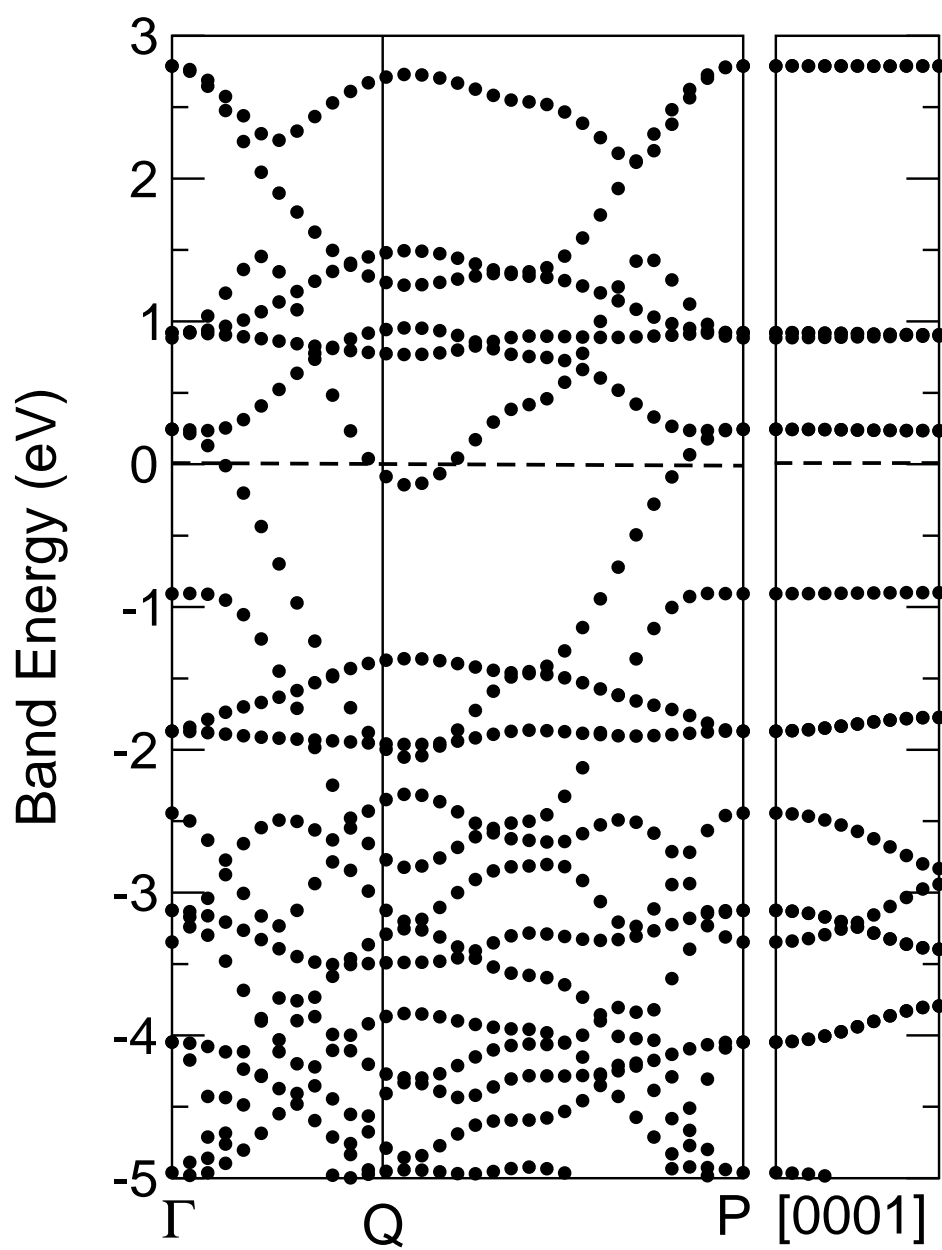




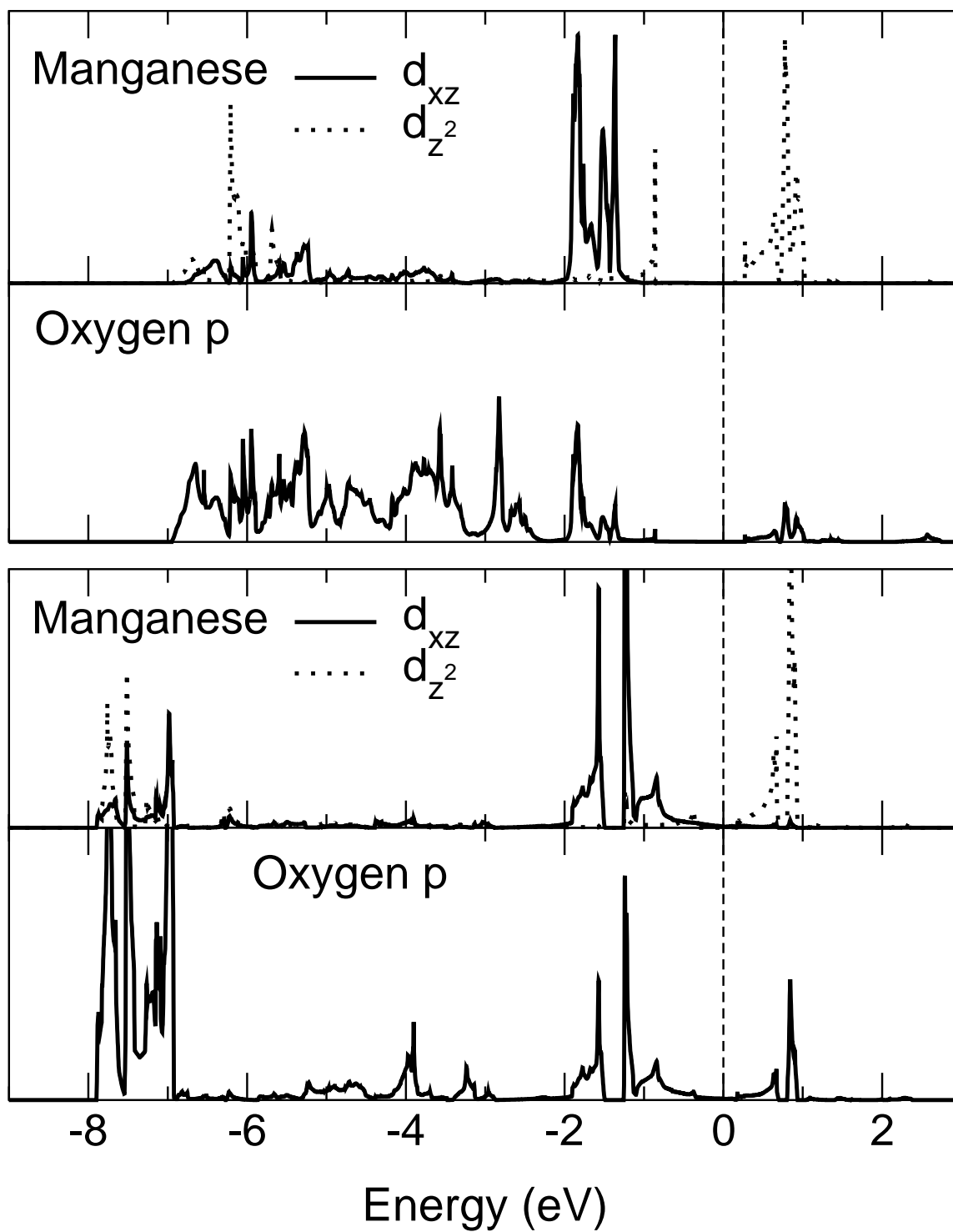


Density of States





Density of States



Densities of States

